Electrical transport and electronic properties of multiband metallic PdSn$_2$

C.-C. Chang [1,2,3] C.-E. Hsu [4] J.-Y. Haung [5] T.-C. Liu,[5] C.-M. Cheng [6,7,8,3] W.-T. Chen [9,10,3] P.-Y. Cheng,[1,2]
C.-N. Kuo,[1,3] C.-S. Lue,[1,3] C.-C. Lee,[4] and C.-L. Huang [1,2,3,*]

[1]*Department of Physics, National Cheng Kung University, Tainan 701, Taiwan*
[2]*Center for Quantum Frontiers of Research & Technology (QFort), National Cheng Kung University, Tainan 701, Taiwan*
[3]*Taiwan Consortium of Emergent Crystalline Materials, National Science and Technology Council, Taipei 10622, Taiwan*
[4]*Department of Physics, Tamkang University, New Taipei 251301, Taiwan*
[5]*Department of Physics, National Tsing Hua University, Hsinchu 30013, Taiwan*
[6]*National Synchrotron Radiation Research Center (NSRRC), Hsinchu 30076, Taiwan*
[7]*Department of Physics, National Sun Yat-sen University, Kaohsiung 80424, Taiwan*
[8]*Department of Electrophysics, National Yang Ming Chiao Tung University, Hsinchu 300 Taiwan*
[9]*Center for Condensed Matter Sciences, National Taiwan University, Taipei 10617, Taiwan*
[10]*Center of Atomic Initiative for New Materials, National Taiwan University, Taipei 10617, Taiwan*

We report the electronic properties of the metallic PdSn$_2$ single crystals by means of electrical resistivity, Hall effect, angle-resolved photoemission spectroscopy (ARPES) measurements and band-structure calculations. A simultaneous two-band analysis is conducted on magnetoresistance (MR) and Hall effect data, revealing hole-carrier dominated transport behavior. ARPES results clearly indicate the multiband nature of PdSn$_2$ with the presence of shallow hole and electron pockets at the Fermi level, supported by first-principles calculations. From the MR data, a breakdown of Kohler's rule in the 300–80 K range is observed. We consider a possible explanation for this phenomenon, which is associated with the temperature-induced band shift near the Fermi surface.

I. INTRODUCTION

Conductors and insulators are conventionally characterized by their electronic band structures. The band evolution near the Fermi level dictates the material's physical properties, including thermodynamic and magnetic properties, as well as electrical transport [1]. Metals display significant band crossings near the Fermi level while, in contrast, insulators feature an energy gap of several electron volts that precludes the presence of electronic states. In semimetals, the band structure exhibits an overlap between the bottom of the conduction bands and the top of the valence bands, leading to a high degree of tunability in the material's physical behavior when tuning parameters are introduced. For example, in the case of the semimetal WTe$_2$, an extremely large increase in resistance occurs when a magnetic field is applied, a phenomenon attributed to perfect carrier compensation [2]. In recent decades, topological semimetals with nontrivial Fermi-surface properties have gained increasing attention. These systems host emergent phenomena, such as high mobility and edge states, originating from high-energy physics, where a Dirac equation was established to describe the motion of particles under the theory of relativity [3–5]. These results suggest a potential application, which prompts the search for unique semimetals and materials with multiple bands where both hole and electron bands cross at the Fermi level.

Elemental tin, its alloys, and intermetallic compounds have not only been used in many technical applications but also exhibit fascinating electronic and physical properties [6]. For example, α-Sn and the intermetallic compound PtSn$_4$ have been reported as topological Dirac semimetals [7,8]. The binary phase diagram of palladium and tin (Pd$_n$Sn$_m$) has been extensively studied, revealing the discovery of at least ten different compositions of Pd$_n$Sn$_m$ [9,10]. On the tin-rich side of the phase diagram, single crystals of PdSn$_m$ with values of $m = 2$, 3, and 4 were successfully grown using the flux method [11,12]. The structures of PdSn$_m$ with $m = 2$, 3, and 4 are closely related, involving the stacking of similar building blocks that form different networks of Sn atoms [11]. To the best of our knowledge, among these compounds, PdSn$_4$ is the only system that has been extensively studied. The physical properties of PdSn$_4$ are reported to be qualitatively similar to those of PtSn$_4$. In fact, PdSn$_4$ also exhibits a significant magnetoresistance (MR) of $8 \times 10^4\%$ at $B = 14$ T and $T = 1.8$ K [12]. This prompts us to investigate PdSn$_2$ in this paper, as it will be interesting to examine whether exotic electronic properties may also emerge, considering the structural similarity among PdSn$_m$ with values of $m = 2$, 3, and 4.

A previous study on polycrystalline PdSn$_2$ revealed the absence of long-range magnetic order and its diamagnetic behavior. The temperature dependence of electrical transport suggests that the system exhibits metallic behavior [13]. In our paper, we conducted extensive MR and Hall effect measurements on a single crystal of PdSn$_2$ and found a violation of Kohler's rule. Angle-resolved photoemission spectroscopy and first-principles calculations are in agreement, revealing that the Fermi level falls within several electron and hole bands. We discuss the potential mechanisms behind the violation of Kohler's rule in PdSn$_2$.

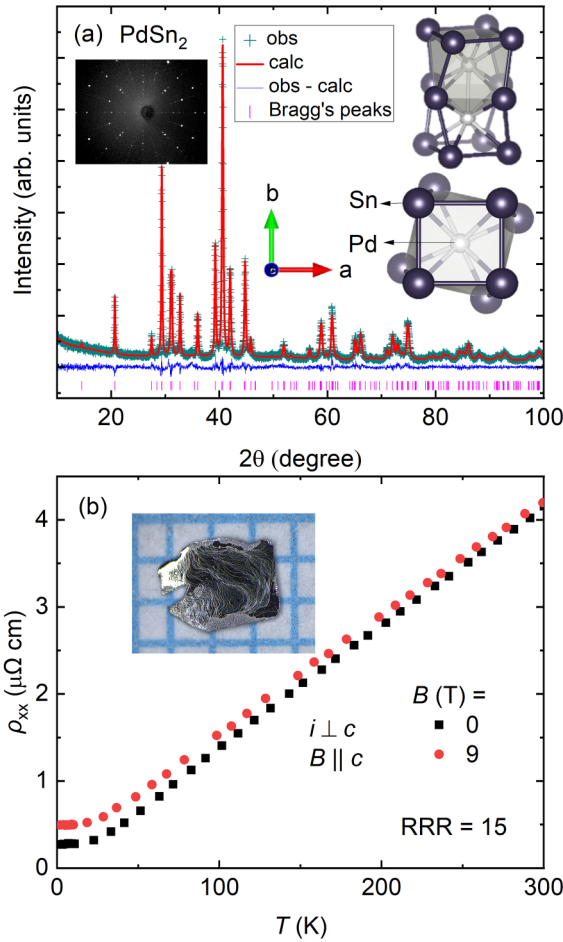*Corresponding author: clh@phys.ncku.edu.tw

FIG. 1. (a) X-ray powder-diffraction pattern of $PdSn_2$ at room temperature. Observed (green cross), calculated (red line), differences (blue line), and Bragg reflections (vertical bars) are labeled. The left inset shows the Laue pattern taken along the tetragonal [001] direction. The upper-right inset shows the respective position of Pd and Sn atoms, where the lower-right inset shows the top view along c axis. (b) Electrical resistivity under field of 0 and 9 T. The inset shows a photo of the crystal for transport measurements.

II. RESEARCH METHODS

Single crystals of $PdSn_2$ were grown through a slow cooling process from a Sn-rich melt following the Pd-Sn binary phase diagram [14]. Pd (99.99%) and Sn (99.99%) raw materials were mixed in a molar ratio of 15:85, sealed in a fused silica ampule under vacuum, and heated to $750\,°C$. The mixture was held at that temperature for 24 hours before being slowly cooled to $400\,°C$ over a period of more than 100 hours. Finally, the excess Sn liquid was separated from the crystals by inverting the tube and centrifuging at $400\,°C$. The resulting crystal has a clear, platelike shape with a shiny surface and typical dimensions of approximately 3 mm× 3 mm× 0.3 mm, as shown in the inset of Fig. 1(b). $PdSn_2$ crystallizes in a tetragonal structure with the space group $I4_1/acd$. Room-temperature powder x-ray diffraction measurement was performed using $CuK\alpha$ radiation (Bruker D2 Phaser) and the data is shown in Fig. 1(a). The crystal structure was analyzed using the Rietveld method with

TABLE I. Crystal data and structure refinement for $PdSn_2$. a and c are lattice parameters. V is the unit-cell volume. R_p and R_{wp} are unweighted and weighted profile R factors, respectively, and GOF represents the goodness of fit obtained from the refinement results. Occ. is occupancy and B_{iso} is the thermal parameter.

Tetragonal $I4_1/acd$ (No. 142)
$a = 6.4894(3)$ Å, $c = 24.354(1)$ Å, V = 1025.6(1) Å³
$R_{wp} = 9.78$, $R_p = 7.54$, GOF = 1.27

Atom	x	y	z	Occ.	B_{iso}	Site
Pd	0	0	0.0578(1)	1	0.23(6)	16d
Sn1	0.25	0.2517(4)	0.125	1	0.32(5)	16e
Sn2	0.1557(2)	0.1557	0.25	1	0.32(5)	16f

the TOPAS suite [15]. The refined structure parameters are consistent with those obtained from the polycrystalline sample [13] and are summarized in Table I. The crystal orientation was confirmed using a Laue x-ray diffraction method. The room-temperature Laue diffractogram demonstrates the high quality of the single-crystalline sample, with an example shown in the inset of Fig. 1(a). Temperature-dependent x-ray powder diffraction data were obtained using a HyPix-6000 HE detector and a molybdenum source with an XtaLAB Synergy-S diffractometer. The pulverized powder sample was packed in a 0.1 mm borosilicate capillary, and the capillary was kept spinning during data collection for data averaging (see Ref. [15]).

Electrical transport properties were studied using a Quantum Design PPMS Dynacool. Five-point contacts enabled simultaneous measurements of resistivity and the Hall effect. A magnetic field of up to 9 T was applied parallel to the c axis, while the current was applied in the ab plane.

Angle-resolved photoemission spectroscopy (ARPES) experiments were conducted at beamline BL21B1 of the Taiwan Light Source within the National Synchrotron Radiation Research Center. High-quality $PdSn_2$ single crystals were cleaved *in situ* under ultrahigh vacuum (UHV) conditions, maintaining a base pressure of 8.9×10^{-11} torr prior to the ARPES measurements. The polarization vector of incident beam was consistently oriented within the angular dispersive plane. ARPES spectra were acquired within a UHV chamber equipped with a Scienta R4000 analyzer, employing an angular resolution set to 0.5 degrees. All spectra were collected at a temperature of 92 K, with photon energy ranging from 37 eV to 57 eV. The overall energy resolution of the measurements exceeded 22 meV.

The first-principles calculations were conducted using the QUANTUM ESPRESSO package within the local density approximation. We adopted experimental lattice parameters obtained at 100 K (see Appendix). We employed ultrasoft pseudopotentials with the valence electronic configurations of Pd $4d^9 5s^2$ and Sn $4d^{10} 5s^2 5p^2$ for the calculations. The kinetic energy cutoff was set to 90 (1080) Ry for expanding the plane-wave wave function (charge density and potential). A $36\times36\times36$ k-point sampling was adopted for the primitive-cell calculation. Using the experimental structure, we verified that the force on each atom was less than 0.006 Ry/Å, and the stress was
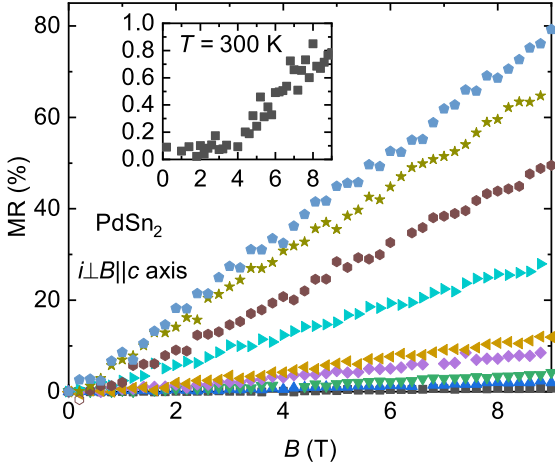
FIG. 2. Isothermal MR measured at, from top to bottom, $T = 2$, 20, 30, 50, 80, 100, 150, 200, and 300 K of PdSn$_2$. An inset highlights the data at 300 K.

FIG. 3. Representative isothermal MR (a) and Hall resistivity (b) of PdSn$_2$. Solid lines are global fits using a two-band model. The legends in (b) are the same as those in (a). A five-point contact configuration is illustrated in the inset of (b). From fits, the mobility (μ) and the carrier density (n) of holes and electrons are summarized in (c) and (d), respectively. $n_{\text{total}} = n_e + n_h$ is the total carrier density. The error bars are included and the length of them is smaller than the symbol size. A vertical dashed line represents the temperature at which the temperature dependence of n_{total} changes.

approximately -1.2 GPa, suggesting that further theoretical relaxation of the crystal structure had a minor effect.

III. MAGNETORESISTANCE AND HALL EFFECT

The temperature dependence of the electrical resistivity, ρ_{xx}, of PdSn$_2$ measured at $B = 0$ and 9 T is shown in Fig. 1(b). Upon cooling from room temperature, ρ_{xx} exhibits a linear dependence on temperature, with a residual resistivity ratio RRR $= \rho_{xx}(300 \text{ K})/\rho_{xx}(2 \text{ K}) = 15$. The overall value of ρ_{xx} in our paper is more than three orders of magnitude smaller than that observed in the polycrystalline sample, indicating significantly fewer impurity and imperfection scattering events in our single crystal [13]. Applying a transverse magnetic field of 9 T increases ρ_{xx} while maintaining a similar temperature dependence, with a more pronounced increase observed at lower temperatures.

Figure 2 illustrates the magnetic-field dependence of MR at various temperatures. MR (%) is calculated as $(\rho_{xx}(B) - \rho_{xx}(0))/\rho_{xx}(0) \times 100\%$, where $\rho_{xx}(B)$ and $\rho_{xx}(0)$ represent the resistivity at B and zero field at a fixed temperature, respectively. At room temperature, the MR exhibits a slow growth, proportional to B^2, reaching a small value of approximately 1% at 9T, as shown in the inset of Fig. 2. This behavior aligns with the metallic characteristics inferred from the $\rho(T)$ behavior. Based on Boltzmann's classical electronic transport theory, it suggests that PdSn$_2$ is a good metal with a large Fermi surface [16]. As the temperature decreases, MR increases and becomes linear with respect to the magnetic field, which signifies a departure from conventional metallic behavior. Linear MR has been observed in several systems, spanning from metals to insulators [17–20], and its origin can result from various factors, both classical and quantum [21–26]. The origin of linear MR in PdSn$_2$ remains unclear at the current stage.

Figures 3(a) and 3(b) display representative MR and Hall resistivity ρ_{xy}, respectively, measured at temperatures of 300, 100, 50, and 2 K. A linear relationship between ρ_{xy} and B has been observed over a wide temperature range (100–
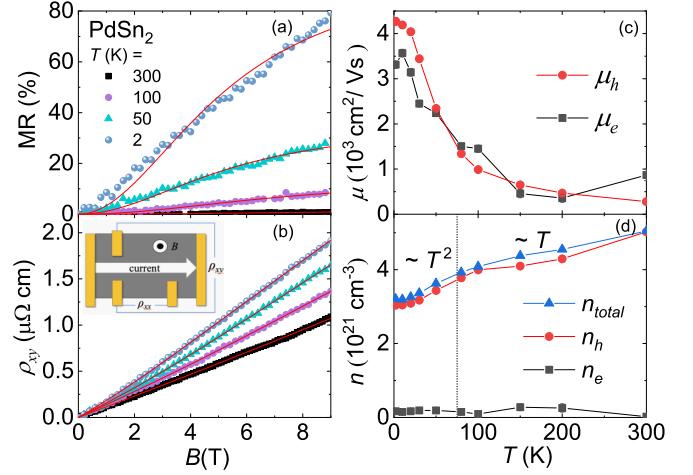
300 K). The positive slope of $\rho_{xy}(B)$ indicates that electrical conduction is dominated by holelike charge carriers. As the temperature decreases, ρ_{xy} gradually increases, nearly doubling at $T = 2$ K compared to 300 K at $B = 9$ T. Below 100 K, $\rho_{xy}(B)$ deviates from linear behavior, suggesting a multiband nature of conduction. Therefore, we adopt a two-band model with one effective electron band and one effective hole band to simultaneously fit ρ_{xx} and ρ_{xy}, i.e.,

$$\rho_{xx}(B) = \frac{1}{e} \frac{(n_h\mu_h + n_e\mu_e) + (n_h\mu_e + n_e\mu_h)\mu_h\mu_e B^2}{(n_h\mu_h + n_e\mu_e)^2 + (n_h - n_e)^2\mu_h^2\mu_e^2 B^2} \quad \text{and} \tag{1}$$

$$\rho_{xy}(B) = \frac{B}{e} \frac{(n_e\mu_e^2 - n_h\mu_h^2) + (n_e - n_h)\mu_h^2\mu_e^2 B^2}{(n_h\mu_h + n_e\mu_e)^2 + (n_h - n_e)^2\mu_h^2\mu_e^2 B^2}, \tag{2}$$

where e stands for elementary charge, n and μ are carrier density and mobility, and the subscript e (or h) denotes electron (or hole). We note that when n_e, n_h, μ_e, and μ_h are treated as free-fitting parameters, there is no global minimum for the fit, and the obtained values are not physically meaningful. We turn to first fit $\rho_{xy}(B)$ with a single band model to determine an initial value of $n = n_h$, i.e., the Hall coefficient

$$R_{\text{H}} = \frac{\rho_{xy}}{B} = \frac{1}{ne} \tag{3}$$

for each temperature. We then assume that the value of n_e is one order of magnitude smaller than the value of n_h. This assumption is based on the observation that ρ_{xy} exhibits nearly linear behavior with respect to B at all temperatures, as shown in Fig. 3(b), indicating dominant hole-type carrier conduction. Finally, the obtained values of n_e and n_h are used as initial parameters, while μ_e and μ_h are left free for the global fit of ρ_{xx} and ρ_{xy} using Eqs. (1) and (2). Applying this methodology yields a global minimum at each temperature. The fitting

results are depicted as solid red curves in Figs. 3(a) and 3(b), and the obtained values of $\mu_{e,h}$ and $n_{e,h}$ are summarized in Figs. 3(c) and 3(d), respectively. We are aware of the limitations in applying the phenomenological two-band model to describe MR and ρ_{xy} using Eqs. (1) and (2). In particular, this model cannot account for the linear MR observed in PdSn$_2$ at low temperatures [see Fig. 3(a)]. Consequently, the uncertainty in the values of μe, h, and $n_{e,h}$ at low temperatures is underestimated when employing the method of least squares.

Between 300 and 100K, both μ_e and μ_h remain nearly constant in temperature, at approximately 10^3 cm^2/V s. Upon further cooling, μ_e and μ_h track each other, increasing by 3–4 times as the temperature decreases to 2 K, suggesting that lattice scattering dominates the mobility [27]. The mobility of PdSn$_2$ is comparable to that of high-purity Si and two orders of magnitude larger than that of conventional metals [28]. In terms of carrier density, while n_e remains nearly constant with temperature and is 20–30 times smaller than n_h throughout the entire temperature range, n_h decreases as the temperature decreases. Between 300 and 100 K, the total carrier density, $n_{\text{total}} = n_e + n_h$, decreases linearly with temperature. At lower temperatures, n_{total} exhibits a quadratic temperature dependence down to 2 K, reaching approximately 3×10^{21} cm^{-3}, which is about 1–2 orders of magnitude smaller than that of typical good metals [29]. The explanation for the change in temperature dependence of the carrier density will be addressed later.

IV. ANGLE-RESOLVED PHOTOEMISSION SPECTROSCOPY AND BAND STRUCTURE CALCULATIONS

To gain deeper insights into the phenomenological two-band model within the PdSn$_2$ system, we conducted an extensive investigation combining ARPES measurements and band-structure calculations. This comprehensive approach allowed us to elucidate the electronic structure of PdSn$_2$ single crystals. We performed ARPES experiments with varying photon energies, ranging from 37 to 57 eV. This energy range was carefully selected to cover multiple periods of the Brillouin zone (BZ) along the k_z direction due to the large lattice constant along the c axis to examine the character of three-dimensional band dispersion behavior [30]. In the photon energy-dependent ARPES experiment, the observed bands did not display clear dispersion behavior. This observation suggests a quasi-two-dimensional band behavior for the observed bands near the Fermi level. Figure 4(a) displays the band mapping results across three BZs derived from ARPES spectra acquired along the direction using a 57 eV photon energy. Evidently, we observed two distinct electron pockets exhibiting Fermi crossings at ±0.17 and ±0.22 Å^{-1} at the Γ point. The smaller (larger) electron pocket is denoted by the red (white) bars on top of Fig. 4(a). Additionally, we identified a holelike band displaying a band crossing at 1.7 Å^{-1} in the third BZ, which intersects with the observed electron pocket at a binding energy of -0.2 eV. To enhance our understanding of the observed band dispersion, Fig. 4(b) presents the calculated band structure, with distinct colors representing orbital spectra corresponding to different orbitals. The Pd bands, which mainly contribute to lower binding energies due to their
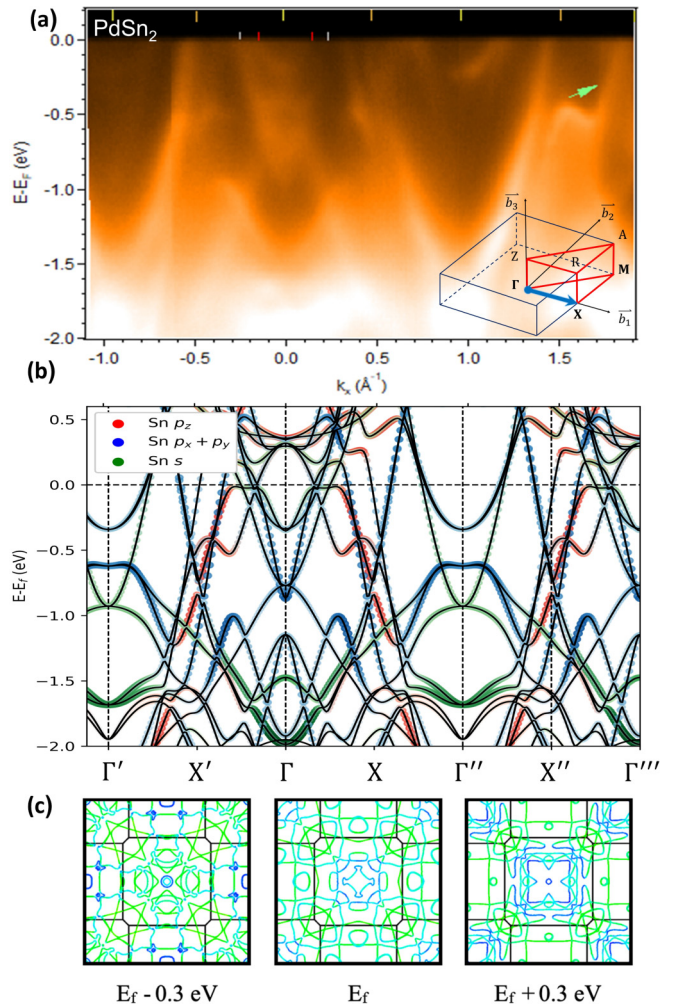

FIG. 4. (a) ARPES spectra of PdSn$_2$ recorded along the direction using a 57 eV photon energy at 92 K. A band crossing at 1.7 Å^{-1} in the third BZ is labeled with green arrow. The inset is the BZ of the conventional cell. A blue arrow marks the path from Γ to X. Yellow and orange vertical bars correspond to high symmetry points on BZ along the $\vec{b}_1$ direction, i.e., Γ and X (also Γ', Γ'', Γ''', X', and X'' in other BZs) noted in (b). (b) First-principles band structure obtained from the primitive-cell calculation along the same path. The contributions of Sn s, $p_x + p_y$, and p_z orbitals are colored by green, blue, and red circles, respectively. Γ', X', Γ, X, Γ'', X'', and Γ''' denote -1, -0.5, 0, 0.5, 1, 1.5, and 2 $\vec{b}_1$, respectively. (c) First-principles Fermi surfaces on the k_x-k_y plane of the primitive-cell BZ at three selected energies relative to the Fermi level.

relatively stable bonding, are distinguishable. Meanwhile, the bands near the Fermi level are primarily attributed to Sn p orbitals. The nature of observed electron pockets could be attributed to the contribution of Sn s and $p_x + p_y$ orbitals, and the holelike bands are originated from Sn $p_x + p_y$ and p_z orbitals. The calculated results qualitatively corroborate the consistency with the ARPES findings, demonstrating that the calculated bands align with the ARPES spectra. For instance, another band crossing of electron and hole bands occurs at ±0.25 Å^{-1} at the Fermi level, and two distinct electron pockets appear in the second BZ. These findings provide evidence that PdSn$_2$ exhibits characteristics of a multiband metal with

the presence of shallow hole and electron pockets at the Fermi level and a metallic Fermi surface, as shown in Fig. 4(c). The observed hole and electron bands further strengthen that the phenomenological two-band model analysis of MR and the Hall effect serves as a good starting point to understand the transport in PdSn$_2$.

V. KOHLER'S RULE TEST

In a conventional metal, the application of a magnetic field causes a charge to move in a circular path, referred to as a cyclotron orbit, which results in an increase in electrical resistance. When there is more scattering in the material, indicated by a higher zero-field resistivity $\rho_{xx}(0)$, fewer cyclotron orbits can be completed when the field is applied, leading to a reduction in MR. This relation is described by Kohler, who stated that MR is a function of the ratio $B/\rho_{xx}(0)$,

$$\mathrm{MR} = \alpha \left[\frac{B}{\rho_{xx}(0)} \right]^m, \tag{4}$$

where α and $m = 1 - 2$ are constants [12,31,32]. Kohler's rule indicates that charge carriers on a single Fermi surface with a single relaxation time dictate the magnetotransport behavior and this principle has been verified in many metallic systems [16,33]. We plot the MR data vs $B/\rho_{xx}(0)$ on a double-logarithmic scale in Fig. 5(a). It clearly demonstrates that the data between $T = 2 - 50$ K collapse onto one branch with $m = 1$ in Eq. (4). As the temperature gradually rises above 50 K, the MR exhibits a gradual departure from the low-temperature data, approaching $m = 2$ at 300 K. This indicates a violation of Kohler's rule in PdSn$_2$.

VI. DISCUSSIONS

The violation of Kohler's rule was also observed in the Weyl semimetal TaP. Xu *et al.* explained that this violation is due to thermally induced changes in carrier density and further proposed an extended Kohler's rule, MR $= f(B/n_{\mathrm{total}}\rho_0)$, to describe the MR of TaP [34]. The extended Kohler's rule takes into account that (1) n_{total} is temperature dependent and (2) the carrier densities and mobilities from different bands have a similar temperature dependence. In PdSn$_2$, μ_h and μ_e closely follow each other, increasing as the temperature decreases, and $n_{\mathrm{total}} \sim n_h$ across the entire temperature range [Figs. 3(c) and 3(d)]. This conforms PdSn$_2$ to the theoretical framework of the extended Kohler's rule. Therefore, we plot MR against $B/n_{\mathrm{total}}\rho_0$ in Fig. 5(b). For the sake of convenience in our discussions, we scale the carrier density to the 300 K curve, i.e., $n_{\mathrm{total}} = 1$ for MR (300 K), by adjusting $n_{n_{\mathrm{total}}}$ for each curve. The plot shows that scaling works slightly better using an extended Kohler's rule than the original Kohler's rule in Fig. 5(a). However, the scaling results in a temperature-dependent power, as demonstrated by the solid black curve in Fig. 5(b), which is not anticipated in the extended Kohler's rule. This suggests that other mechanisms may also contribute to the violation of Kohler's rule in PdSn$_2$.

A variety of physical mechanisms have been proposed to explain the violation of Kohler's rule in different systems, including multiple scattering rates [35–38], a suppression of the density of states at the Fermi energy [39], multiband effects
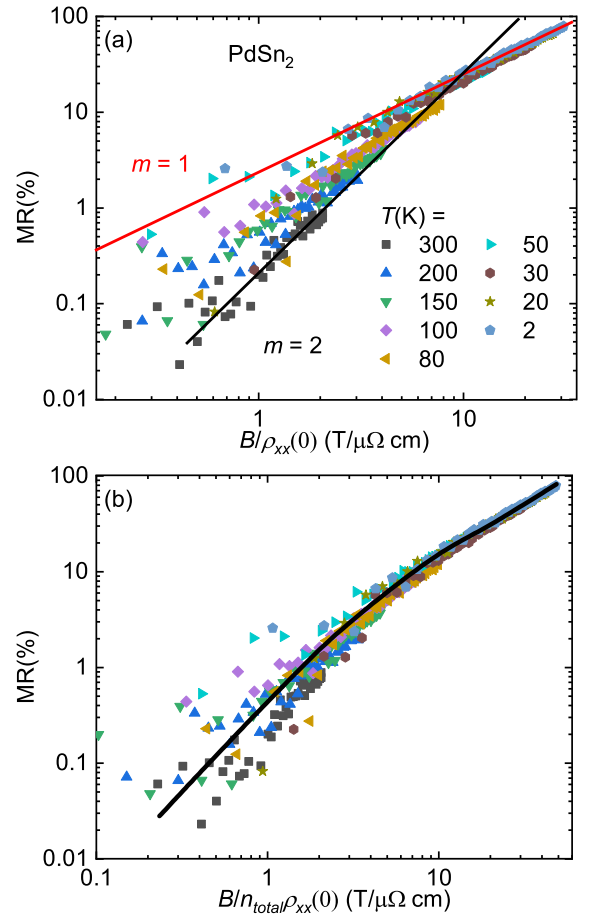

FIG. 5. (a) Kohler's plot. (b) Extended Kohler's rule's plot. See text for details.

[40,41], non-Fermi-liquid behavior [42], and a temperature-induced Lifshitz transition [43]. The anisotropic scattering rate is related to the Hall scattering rate. The Hall angle, $\cot(\theta_H) = \rho_{xx}/\rho_{xy}$, is inversely proportional to the Hall relaxation time, while the relaxation time for longitudinal transport is proportional to $1/\rho_{xx}$. The deviation between the Hall relaxation time and the transport relaxation time leads to the anisotropic scattering rate. Figure 6 demonstrates that ρ_{xx} and $\cot(\theta_H)$ share the same temperature dependence. Therefore, we can eliminate multiple scattering rates as the cause of the violation of Kohler's rule in PdSn$_2$.

Suppression of the density of states occurs as a pseudogap forms at lower temperatures. This phenomenon is commonly observed in iron-based or cuprate superconductors, where the carrier density undergoes significant changes as the pseudogap opens. Such behavior is not observed in PdSn$_2$, as depicted in Fig. 3(d). The multiband effect is associated with the compensation between the contributions of electrons and holes, resulting in a nonlinear relationship between ρ_{xy} and the magnetic field. In the case of PdSn$_2$, transport is primarily dominated by the contribution of holes and, therefore, the violation of Kohler's rule may not link to the multiband effect. Non-Fermi-liquid behavior is often observed in proximity to the magnetic quantum critical point, where the magnetic phase transition is destroyed by quantum fluctuations [44].
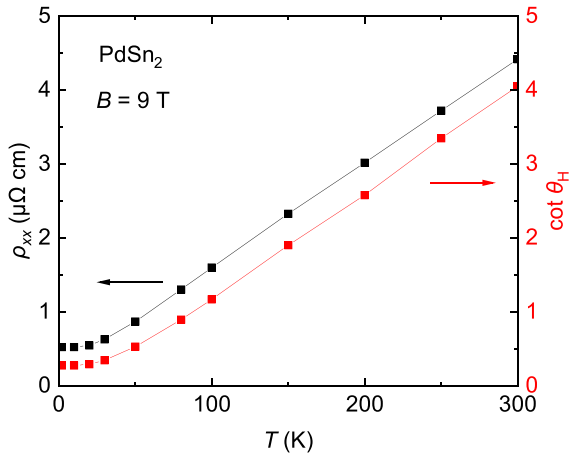
FIG. 6. Temperature dependence of ρ_{xx} and Hall angle $\cot\Theta_H$.

The temperature dependence of the magnetic susceptibility indicates that PdSn$_2$ is diamagnetic, and we found no evidence of non-Fermi-liquid behavior [13].

Finally, let's discuss the case of thermally induced changes in the band structure. Figure 3(d) illustrates that n_{total} vs T exhibits a change in slope around 75 K, below which a quadratic temperature dependence is observed. In the case of a single band, the carrier density decreases as the temperature decreases, owing to the temperature-dependent Fermi-Dirac distribution. That is, the temperature dependence of the carrier density is influenced by the relative position of the Fermi level to the top of the valence band (density of holes) and the bottom of the electron band (density of electrons) [34]. However, when there are two or more bands crossing the Fermi level, the situation becomes complex. Band structure calculations reveal the presence of a few bands at $k_x = \pm 0.2 - 0.3$ Å^{-1}, which are primarily contributed to by Sns and Snpz orbitals and are located very close to the Fermi level. These bands may disappear or shift in proximity to the Fermi level at around 75 K, similar to the situation in a temperature-induced Lifshitz transition [43]. To confirm this hypothesis, future research involving ARPES measurements at lower temperatures is needed to compare the electronic band structure in various temperature ranges.

In summary, we have grown single crystals of PdSn$_2$ using the flux method. Electrical resistivity and Hall effect measurements indicate two-band transport behavior dominated by hole bands. Angle-resolved photoemission spectroscopy measurements and band structure calculations are in agreement, providing support for the multiband nature of PdSn$_2$, with several electron and hole bands lying across the Fermi level. The MR data follows Kohler's rule below 50 K, but it deviates from the universal curve at higher temperatures, possibly due to a temperature-induced band shift. Our results demonstrate that PdSn$_2$ exhibits interesting band structure properties that open the door for future research.

APPENDIX

1. Temperature-dependent x-ray diffraction

The collected patterns were analyzed with Rietveld method using a TOPAS suite. The temperature evolution of the PdSn$_2$ diffraction patterns from 100 to 350 K is shown in Fig. 7(a). No apparent peak splitting or broadening was observed, indicating no symmetry change or phase transition occurred within the measured temperature range. Due to the limit of the resolution obtained from XtaLAB Synergy-S, only lattice constant information was extracted from the refinement. The refined lattice constants and the unit-cell volume against temperature are shown in Figs. 7(b) and 7(c).
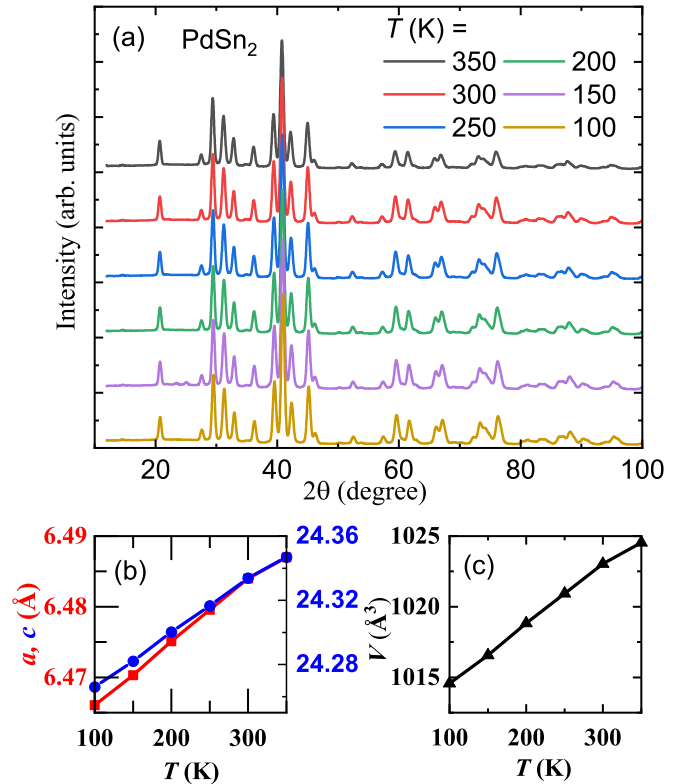

FIG. 7. (a) Temperature dependence of XRD paterns of PdSn$_2$. (b) Temperature dependence of lattice constants and (c) unit-cell volume.

[1] H. Ehrenreich, Band structure and electron transport of GaAs, Phys. Rev. **120**, 1951 (1960).

[2] M. N. Ali, J. Xiong, S. Flynn, J. Tao, Q. D. Gibson, L. M. Schoop, T. Liang, N. Haldolaarachchige, M. Hirschberger, N. P. Ong, and R. J. Cava, Large, non-saturating magnetoresistance in WTe$_2$, Nature (London) **514**, 205 (2014).

[3] T. Liang, Q. Gibson, M. N. Ali, M. Liu, R. J. Cava, and N. P. Ong, Ultrahigh mobility and giant magnetoresistance in the Dirac semimetal Cd$_3$As$_2$, Nat. Mater. **14**, 280 (2015).

[4] S.-Y. Yang, H. Yang, E. Derunova, S. S. P. Parkin, B. Yan, and M. N. Ali, Symmetry demanded topological nodal-line materials, Adv. Phys.: X **3**, 1414631 (2018).

[5] B. Q. Lv, T. Qian, and H. Ding, Experimental perspective on three-dimensional topological semimetals, Rev. Mod. Phys. **93**, 025002 (2021).

[6] R. Pöttgen, Stannides and intermetallic tin compounds—fundamentals and applications, Z. Naturforschung B **61**, 677 (2006).

[7] Y. Wu, L.-L. Wang, E. Mun, D. D. Johnson, D. Mou, L. Huang, Y. Lee, S. L. Bud'ko, P. C. Canfield, and A. Kaminski, Dirac node arcs in PtSn$_4$, Nat. Phys. **12**, 667 (2016).

[8] C.-Z. Xu, Y.-H. Chan, Y. Chen, P. Chen, X. Wang, C. Dejoie, M.-H. Wong, J. A. Hlevyack, H. Ryu, H.-Y. Kee, N. Tamura, M.-Y. Chou, Z. Hussain, S.-K. Mo, and T.-C. Chiang, Elemental topological Dirac semimetal: α-Sn on InSb(111), Phys. Rev. Lett. **118**, 146402 (2017).

[9] H. Okamoto, Pd-Sn (palladium-tin), J. Phase Equilib. Diffus. **33**, 253 (2012).

[10] S. Cui, J. Wang, Z. You, and R. E. Napolitano, Critical evaluation and thermodynamic modeling of the Pd-Sn system, Intermetallics **126**, 106945 (2020).

[11] J. Nylén, F. Garcìa Garcìa, B. Mosel, R. Pöttgen, and U. Häusermann, Structural relationships, phase stability and bonding of compounds PdSn$_n$ (n = 2, 3, 4), Solid State Sci. **6**, 147 (2004).

[12] N. H. Jo, Y. Wu, L.-L. Wang, P. P. Orth, S. S. Downing, S. Manni, D. Mou, D. D. Johnson, A. Kaminski, S. L. Bud'ko, and P. C. Canfield, Extremely large magnetoresistance and Kohler's rule in PdSn$_4$: A complete study of thermodynamic, transport, and band-structure properties, Phys. Rev. B **96**, 165145 (2017).

[13] B. Künnen, D. Niepmann, and W. Jeitschko, Structure refinements and some properties of the transition metal stannides Os$_3$Sn$_7$, Ir$_5$Sn$_7$, Ni$_{0.402(4)}$Pd$_{0.598}$Sn$_4$, α-PdSn$_2$ and PtSn$_4$, J. Alloys Compd. **309**, 1 (2000).

[14] V. A. Baheti, P. Kumar, and A. Paul, Growth of phases in the solid-state from room temperature to an elevated temperature in the Pd-Sn and the Pt–Sn systems, J. Mater. Sci.: Mater. Electron. **28**, 18379 (2017).

[15] A. A. Coelho, TOPAS and TOPAS-Academic: An optimization program integrating computer algebra and crystallographic objects written in C^{++}, J. Appl. Cryst. **51**, 210 (2018).

[16] A. P. Pippard, *Magnetoresistance in Metals* (Cambridge University Press, Cambridge, UK, 1989).

[17] Z. Wang, Y. Sun, X.-Q. Chen, C. Franchini, G. Xu, H. Weng, X. Dai, and Z. Fang, Dirac semimetal and topological phase transitions in A_3Bi (A = Na, K, Rb), Phys. Rev. B **85**, 195320 (2012).

[18] Z. Wang, H. Weng, Q. Wu, X. Dai, and Z. Fang, Three-dimensional Dirac semimetal and quantum transport in Cd$_3$As$_2$, Phys. Rev. B **88**, 125427 (2013).

[19] Z. H. Wang, L. Yang, X. J. Li, X. T. Zhao, H. L. Wang, Z. D. Zhang, and X. P. A. Gao, Granularity controlled nonsaturating linear magnetoresistance in topological insulator Bi$_2$Te$_3$ films, Nano Lett. **14**, 6510 (2014).

[20] S. Mitra, Jeremy Goh Swee Kang, J. Shin, J. Q. Ng, S. S. Sunku, T. Kong, P. C. Canfield, B. S. Shastry, P. Sengupta, and C. Panagopoulos, Quadratic to linear magnetoresistance tuning in TmB$_4$, Phys. Rev. B **99**, 045119 (2019).

[21] A. A. Abrikosov, Quantum magnetoresistance, Phys. Rev. B **58**, 2788 (1998).

[22] J. Hu and T. F. Rosenbaum, Classical and quantum routes to linear magnetoresistance, Nat. Mater. **7**, 697 (2008).

[23] A. Narayanan, M. D. Watson, S. F. Blake, N. Bruyant, L. Drigo, Y. L. Chen, D. Prabhakaran, B. Yan, C. Felser, T. Kong, P. C. Canfield, and A. I. Coldea, Linear magnetoresistance caused by mobility fluctuations in n-doped Cd$_3$As$_2$, Phys. Rev. Lett. **114**, 117201 (2015).

[24] J. C. W. Song, G. Refael, and P. A. Lee, Linear magnetoresistance in metals: Guiding center diffusion in a smooth random potential, Phys. Rev. B **92**, 180204(R) (2015).

[25] T. Khouri, U. Zeitler, C. Reichl, W. Wegscheider, N. E. Hussey, S. Wiedmann, and J. C. Maan, Linear magnetoresistance in a quasifree two-dimensional electron gas in an ultrahigh mobility GaAs quantum well, Phys. Rev. Lett. **117**, 256601 (2016).

[26] F. Kisslinger, C. Ott, and H. B. Weber, Origin of nonsaturating linear magnetoresistivity, Phys. Rev. B **95**, 024204 (2017).

[27] K. Kaasbjerg, K. S. Thygesen, and K. W. Jacobsen, Phonon-limited mobility in n-type single-layer MoS from first principles, Phys. Rev. B **85**, 115317 (2012).

[28] R. A. Logan and A. J. Peters, Impurity effects upon mobility in silicon, J. Appl. Phys. **31**, 122 (1960).

[29] N. W. Ashcroft and N. D. Mermin, *Solid State Physics* (Holt-Saunders, Fort Worth, 1976).

[30] A. Damascelli, Probing the electronic structure of complex systems by ARPES, Phys. Scr. **2004**, 61 (2004).

[31] M. Kohler, Zur magnetischen Widerstandsänderung reiner Metalle, Ann. Phys. **424**, 211 (1938).

[32] Y. L. Wang, L. R. Thoutam, Z. L. Xiao, J. Hu, S. Das, Z. Q. Mao, J. Wei, R. Divan, A. Luican-Mayer, G. W. Crabtree, and W. K. Kwok, Origin of the turn-on temperature behavior in WTe$_2$, Phys. Rev. B **92**, 180402(R) (2015).

[33] E. Fawcett, High-field galvanomagnetic properties of metals, Adv. Phys. **13**, 139 (1964).

[34] J. Xu, F. Han, T.-T. Wang, L. R. Thoutam, S. E. Pate, M. Li, X. Zhang, Y.-L. Wang, R. Fotovat, U. Welp, X. Zhou, W.-K. Kwok, D. Y. Chung, M. G. Kanatzidis, and Z.-L. Xiao, Extended Kohler's rule of magnetoresistance, Phys. Rev. X **11**, 041029 (2021).

[35] J. M. Harris, Y. F. Yan, P. Matl, N. P. Ong, P. W. Anderson, T. Kimura, and K. Kitazawa, Violation of Kohler's rule in the normal-state magnetoresistance of YBa$_2$Cu$_3$O$_{7-\delta}$ and La$_2$Sr$_x$CuO$_4$, Phys. Rev. Lett. **75**, 1391 (1995).

[36] T. Kimura, S. Miyasaka, H. Takagi, K. Tamasaku, H. Eisaki, S. Uchida, K. Kitazawa, M. Hiroi, M. Sera, and N. Kobayashi, In-plane and out-of-plane magnetoresistance in La$_{2-x}$Sr$_x$CuO$_4$ single crystals, Phys. Rev. B **53**, 8733 (1996).

[37] S. Rößler, C. Koz, L. Jiao, U. K. Rößler, F. Steglich, U. Schwarz, and S. Wirth, Emergence of an incipient ordering mode in FeSe, Phys. Rev. B **92**, 060505(R) (2015).

[38] N. Maksimovic, I. M. Hayes, V. Nagarajan, J. G. Analytis, A. E. Koshelev, J. Singleton, Y. Lee, and T. Schenkel, Magnetoresistance scaling and the origin of h-linear resistivity in $BaFe_2(As_{1-x}p_x)_2$, Phys. Rev. X **10**, 041062 (2020).

[39] P. Cheng, H. Yang, Y. Jia, L. Fang, X. Zhu, G. Mu, and H.-H. Wen, Hall effect and magnetoresistance in single crystals of $NdFeAsO_{1-x}f_x$ ($x = 0$ and 0.18), Phys. Rev. B **78**, 134508 (2008).

[40] Y. Sun, T. Taen, T. Yamada, S. Pyon, T. Nishizaki, Z. Shi, and T. Tamegai, Multiband effects and possible Dirac fermions in $Fe_{1+y}Te_{0.6}Se_{0.4}$, Phys. Rev. B **89**, 144512 (2014).

[41] A. Wang, D. Graf, Y. Liu, Q. Du, J. Zheng, H. Lei, and C. Petrovic, Large magnetoresistance in the type-II Weyl semimetal WP_2, Phys. Rev. B **96**, 121107(R) (2017).

[42] S. Nair, S. Wirth, M. Nicklas, J. L. Sarrao, J. D. Thompson, Z. Fisk, and F. Steglich, Precursor state to unconventional superconductivity in $CeIrIn_5$, Phys. Rev. Lett. **100**, 137003 (2008).

[43] Y. Wu, N. H. Jo, M. Ochi, L. Huang, D. Mou, S. L. Bud'ko, P. C. Canfield, N. Trivedi, R. Arita, and A. Kaminski, Temperature-induced Lifshitz transition in WTe_2, Phys. Rev. Lett. **115**, 166602 (2015).

[44] C.-L. Huang, A. M. Hallas, K. Grube, S. Kuntz, B. Spieß, K. Bayliff, T. Besara, T. Siegrist, Y. Cai, J. Beare, G. M. Luke, and E. Morosan, Quantum critical point in the itinerant ferromagnet $Ni_{1-x}Rh_x$, Phys. Rev. Lett. **124**, 117203 (2020).